Atomic-scale mapping of pressure-induced deformations and phase defects in the charge density wave order parameter

M. K. Kinyanjui,[1,*] J. Ebad-Allah,[2,3] M. Krottenmüller,[2] and C. A. Kuntscher[2]

[1]*Electron Microscopy Group of Materials Science, Ulm University, Albert-Einstein Allee 11, 89081 Ulm, Germany*

[2]*Experimental Physics II, Institute of Physics, University of Augsburg, Universitätsstrasse 1, 86159 Augsburg, Germany*

[3]*Department of Physics, Tanta University, 31527 Tanta, Egypt*

(Received 22 June 2021; revised 30 July 2021; accepted 3 August 2021; published 7 September 2021)

Understanding the intricate interplay between multiple electronic phases in quantum materials such as charge density wave (CDW), superconducting, and metallic phases is a challenging issue. Systematic introduction of pressure is one approach that has been used to probe this interplay. However, the influence of pressure together with the intricate interaction between electronic and lattice degrees of freedom can trigger complex structural evolution and distribution of various electronic phases at the atomic scale, the characterization of which demands high spatial resolution. We investigate the atomic-scale response of the charge density waves and the underlying atomic lattice in $1T$-TaS_2 after exposure to hydrostatic pressure. High-resolution transmission electron microscopy images show that the CDW order parameter reacts with an elasticlike strain response to pressure-induced stacking faults and dislocations in the lattice. This is characterized by a proliferation of phase defects including CDW dislocations, discommensurations, and domain walls. Our results evidence the importance of pressure-induced lattice deformations and defects in modulating, stabilizing, or destroying electronic phases at the atomic scale.

DOI: 10.1103/PhysRevB.104.125106

I. INTRODUCTION

The charge density wave (CDW) is an electronic phase observed in many quantum materials, which is characterized by a periodic modulation of electron density that may arise from Fermi-surface instability or electron-phonon interactions [1–3]. The CDW is accompanied by a periodic lattice distortion (PLD), i.e., a modulation of the atomic positions, and the opening of an energy gap (2Δ). The CDW state is characterized by a modulation of the charge density according to

$$\rho(\mathbf{r}) = \rho_0 + \Delta\cos[\mathbf{q}\cdot\mathbf{r} + \varphi(\mathbf{r})]\ldots, \tag{1}$$

where ρ_0 is a constant, Δ is the amplitude, $\mathbf{q}$ is the wave vector, and φ is the phase. The CDW can also be represented by the complex order parameter $\Psi = \Delta e^{i\varphi}$ [2]. The phase φ is related to the position of the CDW in relation to the underlying lattice, while the amplitude Δ is related to the energy gap as well as the amplitude of the atomic displacement. The CDW state is often observed in some weakly and strongly correlated quantum materials, for example, low-dimensional transition metal dichalcogenides, rare-earth tritellurides, and high-temperature cuprate superconductors [1,4–7]. The nature and character of the CDW in these materials are however strongly dependent on their dimensionality, structure, temperature, doping, pressure, intercalation, or the presence of defects [1,8–19]. Additionally, in many quantum materials the CDW phase is often found in competition or coexistence with other electronic phases such as spin density wave, metallic, Mott-insulating, superconducting (SC), antiferromagnetic, or pseudogap phases [4–6]. In particular, the competition/coexistence of CDW and SC phases observed in cuprates and iron-based superconductors has received considerable attention [6,7,9,19–22]. Understanding the interplay between these electronic phases is one of the most challenging problems in solid state research [4–6].

Systematic introduction of pressure is an established experimental approach that has been used to probe the nature of the relationship between CDW and SC phases [8,12–14,18,19]. In several cases, pressure is known to either promote or suppress the CDW phase and hence influence the character of superconductivity or other electronic phases in the materials. Also, it has become clear that quantum materials showing competing electronic phases are often characterized by structural or electronic fluctuations and inhomogeneities at various energy, time, and spatial scales. With respect to spatial scales the phase inhomogeneities can range from nano- to mesoscale [4,23–27]. As such, the application of pressure for probing the interplay of the competing electronic phases is also expected to influence the spatial electronic phase separation [19]. Indeed, the transformation of CDW systems to superconductivity under pressure has been attributed to CDW fluctuations and spatial CDW phase separations [11]. It is thus crucial to understand how pressure affects the structure of the underlying atomic lattice and consequently the nature and the structure of the ordered electronic phases at the atomic scale.

The response of quantum materials to pressure is complex, encompassing changes in inter- or intralayer atomic distances with associated changes in bond lengths, bond angles, coordination, and ultimately electronic structure [8,28,29]. Although

*michael.kinyanjui@uni-ulm.de

the application of hydrostatic pressure is known to cause far less chemical disorder to the material as compared to doping, associated stress can also lead to structural phase transitions and structural defects like stacking faults, twins, or dislocations [30–32]. This is due to the fact that most materials contain intrinsic structural defects and disorder that can have profound influence on the effects of pressure. In this paper we aim to understand the influence of pressure on the lattice structure and subsequently on the CDW order parameter in $1T$-TaS_2 at the atomic scale. This includes the influence of atomic-scale deformations, structural defects, and associated strain fields. Our main results are summarized as follows.

(1) We find that pressure application results in proliferation of lattice defects in the atomic lattice such as stacking faults and partial dislocations.

(2) The elasticlike response of the CDW order parameter to these lattice defects and associated strain field results in local variations in the magnitude of the CDW wave vector and phase defects in the form of CDW dislocations, domain walls, and discommensurations.

II. EXPERIMENTAL DETAILS

The $1T$-TaS_2 single crystals used in this paper were obtained from HQ graphene. A commercial Diacell CryoDAC-Mega (AlmaxEasy-Lab) diamond-anvil cell (DAC) was used to generate the pressure of 2.5 GPa. The sample was placed in the hole of a CuBe gasket inside the DAC. A methanol-ethanol alcohol mixture (4:1) served as hydrostatic pressure transmitting medium. The pressure was determined using the ruby luminescence technique [33,34]. Pristine samples and pressurized samples for transmission electron microscopy (TEM) investigations were prepared to a thickness of a few layers using mechanical exfoliation. The obtained thin layers were then transferred onto perforated carbon sample grids for TEM investigations. High-resolution TEM (HRTEM) imaging and electron diffraction investigations were done on a Titan 80–300 kV and operating at 80 kV.

HRTEM images obtained from pressurized samples were used to determine atomic-scale two-dimensional (2D) strain in the atomic lattice as well as in the CDW order parameter after application of pressure [35,36] (see Supplemental Material [37] for details about the analysis of the HRTEM images). This approach is justified due to two reasons; first, atomic-scale HRTEM or scanning tunneling microscopy images obtained from charge-ordered or modulated structures allow one to separate the contributions from the underlying atomic lattice and from the charge ordering superstructure or electronic phases [19–23,38–41]. This fact enables changes occurring in both lattices due to pressure to be examined separately as well as the correlation between them. Second, ordered electronic phases, including the CDW, can be approximated as crystallized electrons that display elastic response to structural changes in the underlying atomic lattice like a real crystal. This elastic response can be described using strain as well as electronic phase defects including dislocations and domain boundaries [2,42,43]. Using this approach, we determined the displacement field $\mathbf{u}(\mathbf{r})$ of the atomic lattice and the CDW order parameter individually with respect to perfect reference periodic lattices. The derivative of the displacement field $\mathbf{u}(\mathbf{r})$ then gives the 2D atomic-scale deformation tensor (ϵ_{ij}) and in-plane rigid body rotation (ω_{xy}) [35,36].

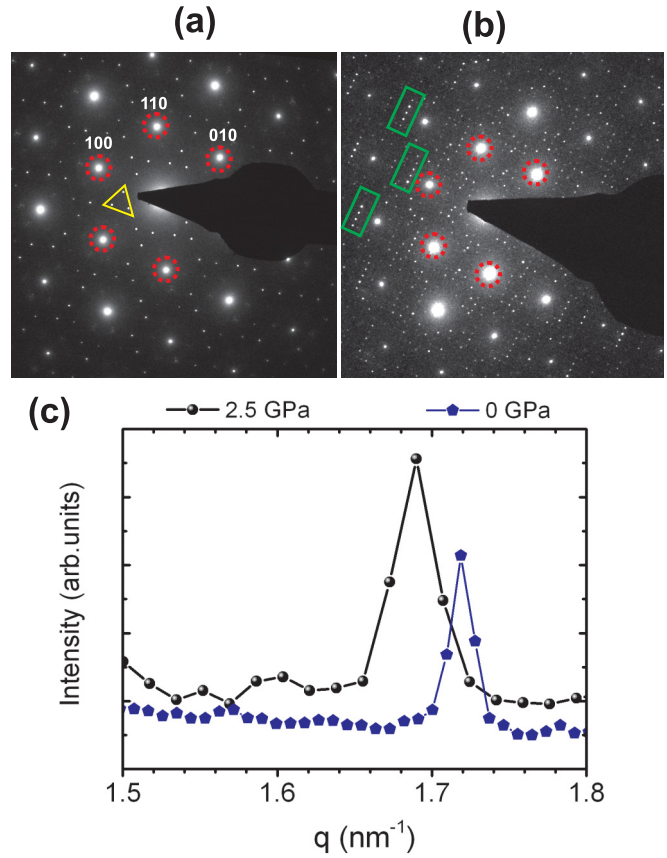

FIG. 1. (a) Electron diffraction pattern for $1T$-TaS_2 obtained at room temperature and zero pressure. The pattern shows Bragg diffraction spots from the atomic lattice (110, 100, 010, dotted circles) and from the second-order superlattice spots arising from the nearly commensurate CDW modulation (marked with a triangle). (b) After applying a hydrostatic pressure of 2.5 GPa. The rectangles mark the streaking observed after pressure application. (c) Comparing the positions of the second-order CDW superlattice peak positions before (0 GPa) and after applying pressure (2.5 GPa).

III. RESULTS AND DISCUSSION

A. Atomic lattice deformations and defects arising from hydrostatic pressure application

In Fig. 1(a) we present an electron diffraction pattern obtained from $1T$-TaS_2 before pressure application. The displayed diffraction pattern is characterized by Bragg spots (110, 100, 010, dotted circles) arising from the underlying atomic lattice as well as the second-order superlattice spots (triangle) due to the nearly commensurate (NC-CDW) modulation characteristic for $1T$-TaS_2 at 300 K. The NC-CDW pattern in $1T$-TaS_2 arises from three CDW/PLDs with a wave vector $\mathbf{q}_{nc} \approx 0.245\mathbf{a}_0^* + 0.068\mathbf{b}_0^* + \frac{1}{3}\mathbf{c}_0^*$ and rotated 12° from the $10\bar{1}0$ direction [1,44–46]. The second-order superlattice reflections from the NC-CDW (marked by triangles) are however the most important and used for the analysis presented here [45–47]. After applying a hydrostatic pressure of 2.5 GPa, the corresponding electron diffraction pattern

[see Fig. 1(b)] is characterized by prominent streaking (marked by rectangles). In Fig. 1(c) we compare the position and width of the second-order CDW superlattice spots (q_i) before (0 GPa) and after applying pressure. Two observations can be made: First, the position of the CDW superlattice spot is shifted after pressure application. Second, the CDW superlattice peaks are broadened in the pressurized sample. The electron diffraction results of pressurized 1T-TaS_2 thus evidence characteristic changes including peak streaking, peak shift, and broadening. As we demonstrate in the following sections, the streaking is a result of the deformation lattice defects that arise as a response to the applied pressure. The broadening and shift in the position of the CDW superlattice peaks indicate changes in the phase, compression-expansion, and the presence of defects in the CDW electronic phase [48]. In the following we use atomic-scale HRTEM images to understand the nature of these deformation defects both in the atomic lattice and in the CDW order parameter in detail.

The HRTEM image in Fig. 2(a) shows the layer structure and stacking along the c ([001]) direction of the sample after pressure application. The corresponding Fourier transform (FT) pattern [Fig. 2(b)] is characterized by Bragg spots with prominent streaking along the [001] direction. The HRTEM image in Fig. 2(c) presents the layer structure in magnified details. In order to understand the deformation defects displayed in the image, fringes representing the (010) lattice planes are visualized by selecting the 010 Bragg spots in the FT pattern with a Gaussian mask followed by the inverse FT. The resulting fringe image [Fig. 2(d)] shows that the lattice fringes are characterized by a stacking fault (marked with an arrow). The deformation effect of the stacking fault gives rise to the bending of the lattice fringes [see Fig. 2(d)]. The structure of an individual stacking fault and associated dislocation are depicted in greater details in the HRTEM and fringe images [Figs. 2(e) and 2(f), respectively]. The calculated shear strain field ϵ_{xy} in the vicinity of these structural defects is displayed in Fig. 2(g), where the position of the dislocation core associated with the stacking fault is marked with a circle. According to the strain map, high strain is found in the vicinity of the stacking fault and the dislocation core.

Here, we briefly discuss the nature of stacking faults observed in 1T-TaS_2 under pressure deformation: The compound 1T-TaS_2 belongs to the CdI_2 structure type which consists of a layer of Ta atoms sandwiched between two layers of hexagonally close packed S atoms [1]. The layer stacking is described as the ABCABC type layer stacking of the S-Ta-S layers. The Ta and S layers are bonded by strong bonds, whereas two adjacent S layers are held together by weak van der Waals bonds. In the CdI_2-type layered crystals, multiple type deformation stacking faults can be induced by pressure [49–53], which are created by a slip between adjacent S layers. This slip also produces edge dislocations lying in the basal plane and having Burger's vector $\mathbf{a}/3\langle 1010\rangle$. These are the stacking faults and dislocations deduced from the HRTEM imaging and electron diffraction results presented here.

B. Effects of the lattice deformations and defects on the CDW order parameter

In the following, we examine how the local structure of the CDW order parameter is modified by the lattice deformations

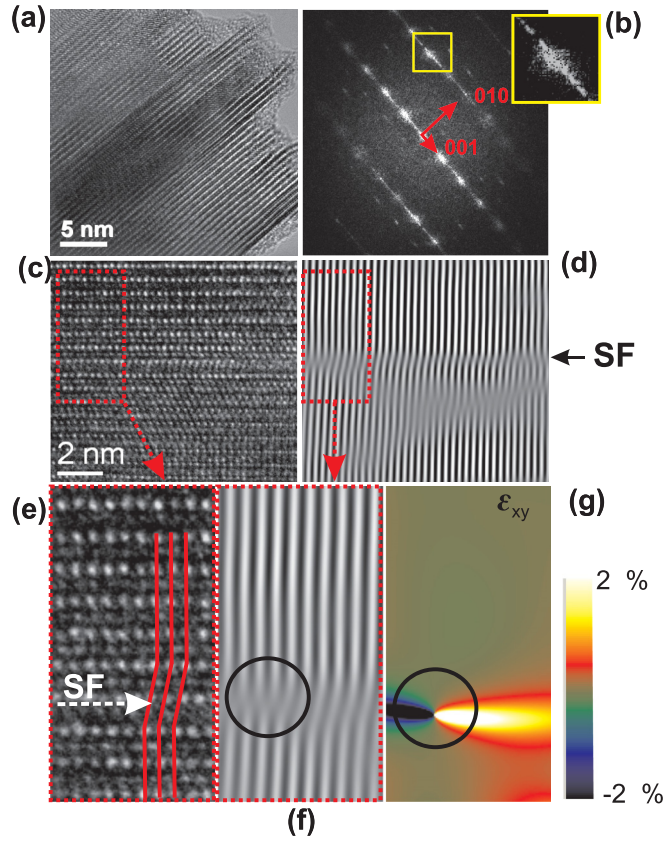

FIG. 2. (a) HRTEM image of the layer structure along the [001] direction after pressure application. (b) FT of the HRTEM image. The inset displays the streaking in the Bragg spots. (c) HRTEM image showing the layer structure in greater details. (d) Lattice fringes from the (010) atomic planes obtained by selecting the 010 Bragg spot [depicted in (b)] with a Gaussian mask followed by inverse FT. A stacking fault (SF) is marked with an arrow. (e) Zoomed region of the HRTEM image showing the SF position. (f) (010) lattice fringes in the region with a SF and a dislocation. (g) Calculated shear strain ϵ_{xy} in the vicinity of the SF and dislocation. The strain scale ranges from + 2 to – 2%, where regions with high strain correspond to high intensity and vice versa. The position of the dislocation core is marked with a circle.

and the strain fields described above. To this end, we obtained and analyzed HRTEM images of the layer structure parallel to the basal *ab* plane [see Fig. 3(a)], as the structural modulation due to the CDW/PLD is largest for the *ab* plane [44]. In addition, pressure-induced structural deformations can be characterized by stacking faults and the associated partial edge dislocations mainly in the basal plane. We therefore expect the effects of structural deformations on the CDW order parameter to be more prominent in the basal plane of the pressurized sample. The HRTEM image of the *ab* plane [see Fig. 3(a)] is indeed characterized by prominent deformation defects. In the corresponding FT pattern [Fig. 3(b)] the Bragg spots from the atomic lattice (circles), as well as the first-order (squares) and second-order (triangle) superlattice spots arising from the CDW/PLD modulation, have been marked. We also calculated the lattice strains, in order to characterize the lattice distortions due to pressure-induced defects. The strain maps in

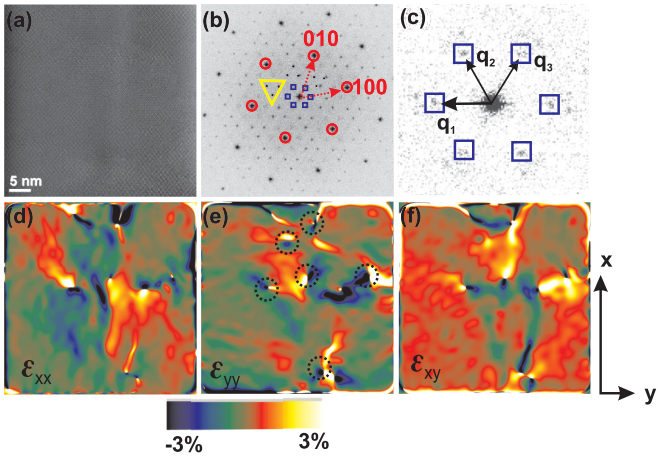

FIG. 3. (a) HRTEM image obtained perpendicular to the [001] direction with deformation defects in the layer plane. (b) Fourier transform (FT) of the HRTEM image with the Bragg spots from the underlying atomic lattice (marked with circles) as well as first- (square) and second-order (triangle) superlattice spots from the CDW/PLD modulation. (c) First-order superlattice reflections q_1, q_2, and q_3 depicted in greater details. Color maps showing the calculated strain profiles in the atomic lattice along the (d) x direction, ϵ_{xx}, and (e) y direction, ϵ_{yy}. (f) Shear strain ϵ_{xy}. The intensity in the color maps represents strain values in the range -3.0 to 3.0%, where regions with high strain correspond to a high intensity and vice versa. The dotted circles indicate the presence of dislocation cores.

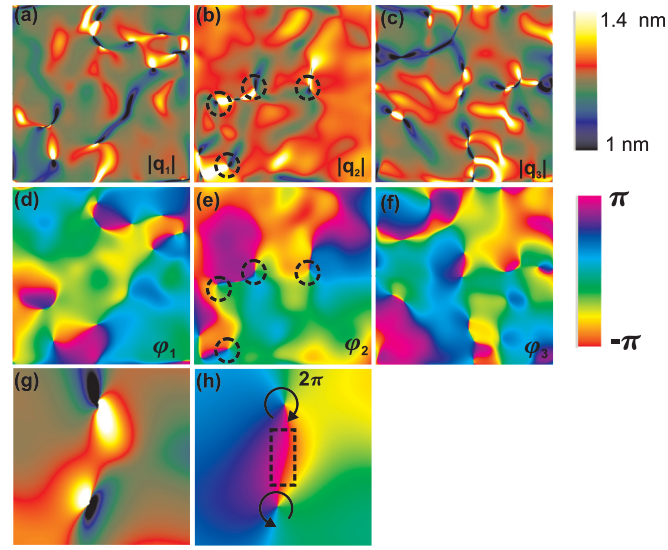

FIG. 4. Intensity maps representing the (a)–(c) magnitude $|q|$ and (d)–(f) phase φ of the individual CDW wave vectors q_1, q_2, and q_3, respectively. The high and low intensity of the color maps, respectively, corresponding to elongated or shortened CDW wave vector with respect to the unstrained parameter. The color scale in the phase images ranges from $-\pi$ to π. The dotted circles in (b) and (e) indicate the positions of the dislocation cores and phase singularities, respectively. (g) Magnitude and (h) phase in the vicinity of a pair of CDW dislocation cores.

Figs. 3(c)–3(e) show the lattice strain profiles for the underlying atomic lattice along the x direction (ϵ_{xx}), y direction (ϵ_{yy}), and shear strain (ϵ_{xy}), respectively. The dotted circles mark the positions of the dislocation cores which appear as singularities in the strain map. The obtained strain maps clearly demonstrate that the atomic lattice is highly deformed due to stacking faults and the associated dislocation networks and their respective strain fields.

We then determined how the magnitudes ($|q|$) and phases φ for individual CDW wave vectors are locally modulated by the atomic-scale deformations and defects, and the associated strain field. This is possible, since HRTEM image and electron diffraction are sensitive to the atomic position modulation that arises from the PLD. Strong coupling of lattice and electronic degrees of freedom means that changes in lattice structure due to the applied pressure or strain from the deformation defects will also have an effect on the structure of the CDW electronic ordered state. It can be shown that the variation in the CDW/PLD phase φ due to strain also leads to local variations of the CDW/PLD wave vector, i.e., $\Delta Q_x = \partial\varphi/\partial x$, $\nabla\varphi = \partial\mathbf{Q}$ [42,54,55]. Since the wave vector and the phase of the PLD can be accessed from the HRTEM image and its FT, the pressure-induced effects on the CDW/PLD phase can be mapped. Hence, the HRTEM image of the pressurized and CDW modulated $1T$-TaS_2 lattice [Fig. 3(a)] can be decomposed into contributions arising from the underlying atomic lattice and those arising from the CDW/PLD modulation. The latter contributions cause the Bragg reflections from the atomic structure as well as the superlattice reflections representing the CDW periodicities q_1, q_2, and q_3 in the FT transform of the HRTEM image [see Fig. 3(b)]. By using a Gaussian mask placed around individual Bragg reflections as well as the superlattice spots q_i in the FT pattern, individual phase images from individual spots can be calculated. These phase images contain information on the variations in the local phase of the atomic lattice as well as the CDW order parameter. In the absence of structural changes or defects, the phase of the lattice fringes from the underlying atomic lattice and the CDW order parameter will be constant. In contrast, structural changes in the underlying atomic lattice and CDW order parameter will result in a variation of the corresponding lattice and superlattice periodicities and consequently introduce phase variations.

The so-obtained magnitudes $|q|$ of the second-order CDW wave vector, q_1, q_2, and q_3, are displayed in Figs. 4(a)–4(c), respectively. The high (low) intensity in the magnitude images shows the elongated (shortened) CDW wave vector with respect to the pristine wave vector. The corresponding phases are shown in Figs. 4(d)–4(f), respectively. The following information can be deduced from the magnitude and phase maps.

(i) The magnitude of the CDW wave vector $|q|$ varies across the structure, characterized by regions with unstrained, elongated, and contracted CDW wave vectors. This variation results from pressure-induced structural deformations, defects, and associated strain fields observed in the underlying atomic structure.

(ii) Similarly, the phase maps of all CDW order parameters have a rich structure, mostly characterized by proliferation of topological phase defects including CDW domain walls, discommensurations, and vortices/dislocations.

The domain walls separate CDW domains, where the phase of the CDW order parameter changes by $+2\pi$ or -2π. In this case the phase within the domain is constant but changes at the domain wall. The second defect we can detect is known as discommensuration [14,19,43,56]. Similar to the domain wall, the phase of the CDW changes across a discommensuration with the only difference being that the amplitude of the CDW remains constant. In contrast, both the phase and amplitude of the CDW change across a domain wall [14]. The third type of topological defects includes CDW vortices/dislocations [14,19,43,56]. CDW dislocations are identified as singularities in the phase maps [9,14,19]. The amplitude of the CDW order parameter is zero at the dislocation core, while its phase winds by 2π around the dislocation. In Figs. 4(g) and 4(h) we plot the magnitude and the corresponding phase of the CDW order parameter in the vicinity of two CDW dislocation cores.

According to the present results and previous reports, the application of hydrostatic pressure causes several effects in the underlying $1T$-TaS_2 atomic lattice, namely, changes in interlayer and interatomic distances, the formation of structural defects in the atomic lattice, and the introduction of lattice strain due to changes in the atomic structure and deformation defects. The CDW order parameter responds to these changes in terms of CDW strain, which leads to local changes in the modulation wave-vector and phase defects in the form of CDW dislocations, discommensurations, and domain walls. Regarding the local effects of atomic-scale defects on the CDW order parameter, our experimental results can be explained by the nature of interactions between the CDW phases with lattice deformations and structural defects, resulting in the pinning of the CDW by the defects. This can be either weak and strong pinning [2,42,43]. For strong pinning the impurity potential is more dominant than the elastic energy of the CDW. The phase of the CDW is therefore locally pinned at the impurity/defect. For weak pinning the elastic deformation energy of the CDW dominates the impurity potential. This pinning induces strain in the CDW lattice, since the CDW reacts elastically by deforming around the defect. When this elastic deformation is no longer sufficient to overcome the pinning energy, formation of phase defects such as dislocations is observed. The number of these CDW defects will also increase with increasing number of defects in the underlying lattice. In such a case the CDW breaks into smaller domains, thus losing its long-range order.

IV. CONCLUSION

In conclusion, we have investigated the atomic-scale response of the CDW order parameter to hydrostatic pressure. By real-space, atomic-scale transmission electron microscopy imaging, the influence of pressure on the structural properties of $1T$-TaS_2 and consequently its influence on the nature and the structure of the CDW was determined at the atomic scale. We find that pressure induces lattice deformations, defects in the form of stacking faults and dislocations, and their associated strain fields. These lead to strong atomic-scale modulation of the CDW order parameter characterized by large strain, and proliferation of phase defects including dislocations, domain walls, and discommensurations in the CDW electronic phase. We show that atomic-scale deformations and defects induced by pressure can have a considerable influence on the local structure of ordered electronic phases, which needs to be taken into account for understanding the effects of pressure in quantum materials.

ACKNOWLEDGMENTS

M.K.K. acknowledges funding from the Deutsche Forschungsgemeinschaft (DFG), Germany, within Grant No. KI 2546/1-1.

[1] J. A. Wilson, F. J. Di Salvo, and S. Mahajan, Adv. Phys. **24**, 117 (1975).
[2] J. McCarten, D. A. DiCarlo, M. P. Maher, T. L. Adelman, and R. E. Thorne, Phys. Rev. B **46**, 4456 (1992).
[3] B. Keimer and J. E. Moore, Nat. Phys. **13**, 1045 (2017).
[4] E. Fradkin, S. A. Kivelson, and J. M. Tranquada, Rev. Mod. Phys. **87**, 457 (2015).
[5] B. F. Hu, B. Cheng, R. H. Yuan, T. Dong, and N. L. Wang, Phys. Rev. B **90**, 085105 (2014).
[6] S. M. Souliou, H. Gretarsson, G. Garbarino, A. Bosak, J. Porras, T. Loew, B. Keimer, and M. Le Tacon, Phys. Rev. B **97**, 020503(R) (2018).
[7] W. D. Wise, M. C. Boyer, K. Chatterjee, T. Kondo, T. Takeuchi, H. Ikuta, Y. Wang, and E. W. Hudson, Nat. Phys. **4**, 696 (2008).
[8] R. H. Friend, R. F. Frindt, A. J. Grant, A. D. Yoffe, and D. Jerome, J. Phys. C **10**, 1013 (1977).
[9] J.-I. Okamoto, C. J. Arguello, E. P. Rosenthal, A. N. Pasupathy, and A. J. Millis, Phys. Rev. Lett. **114**, 026802 (2015).
[10] B. Sipos, A. F. Kusmartseva, A. Akrap, H. Berger, L. Forró, and E. Tutiš, Nat. Mater. **7**, 960 (2008).
[11] Y. I. Joe, X. M. Chen, P. Ghaemi, K. D. Finkelstein, de la Peña, G. A., Y. Gan, J. C. T. Lee, S. Yuan, J. Geck, G. J. MacDougall, T. C. Chiang, S. L. Cooper, E. Fradkin, and P. Abbamonte, Nat. Phys. **10**, 421 (2014).
[12] S. Ravy, C. Laulhé, J.-P. Itié, P. Fertey, B. Corraze, S. Salmon, and L. Cario, Physica B **407**, 1704 (2012).
[13] T. Ritschel, J. Trinckauf, G. Garbarino, M. Hanfland, M. v. Zimmermann, H. Berger, B. Büchner, and J. Geck, Phys. Rev. B **87**, 125135 (2013).
[14] Á. Pásztor, A. Scarfato, M. Spera, C. Barreteau, E. Giannini, and C. Renner, Phys. Rev. Res. **1**, 033114 (2019).
[15] S. Yan, D. Iaia, E. Morosan, E. Fradkin, P. Abbamonte, and V. Madhavan, Phys. Rev. Lett. **118**, 106405 (2017).
[16] S. Gao, F. Flicker, R. Sankar, H. Zhao, Z. Ren, B. Rachmilowitz, S. Balachandar, F. Chou, K. S. Burch, Z. Wang, J. van Wezel, and I. Zeljkovic, Proc. Natl. Acad. Sci. USA **115**, 6986 (2018).
[17] Y. Feng, J. van Wezel, J. Wang, F. Flicker, D. M. Silevitch, P. B. Littlewood, and T. F. Rosenbaum, Nat. Phys. **11**, 865 (2015).
[18] H.-H. Kim, S. M. Souliou, M. E. Barber, E. Lefrancois, M. Minola, M. Tortora, R. Heid, N. Nandi, R. A. Borzi,

G. Garbarino, A. Bosak, J. Porras, T. Loew, M. König, P. J. W. Moll, A. P. Mackenzie, B. Keimer, C. W. Hicks, and M. Le Tacon, Science **362**, 1040 (2018).
[19] A. Mesaros, K. Fujita, H. Eisaki, S. Uchida, J. C. Davis, S. Sachdev, J. Zaanen, M. J. Lawler, and E.-A. Kim, Science **333**, 426 (2011).
[20] Z. Ren, H. Li, H. Zhao, S. Sharma, Z. Wang, and I. Zeljkovic, Nat. Commun. **12**, 10 (2021).
[21] M. H. Hamidian, S. D. Edkins, C. K. Kim, J. C. Davis, A. P. Mackenzie, H. Eisaki, S. Uchida, M. J. Lawler, E.-A. Kim, S. Sachdev, and K. Fujita, Nat. Phys. **12**, 150 (2016).
[22] Q. Zheng, N. J. Schreiber, H. Zheng, J. Yan, M. A. McGuire, J. F. Mitchell, M. Chi, and B. C. Sales, Chem. Mater. **30**, 7962 (2018).
[23] P. Giraldo-Gallo, Y. Zhang, C. Parra, H. C. Manoharan, M. R. Beasley, T. H. Geballe, M. J. Kramer, and I. R. Fisher, Nat. Commun. **6**, 8231 (2015).
[24] G. Campi, A. Bianconi, N. Poccia, G. Bianconi, L. Barba, G. Arrighetti, D. Innocenti, J. Karpinski, N. D. Zhigadlo, S. M. Kazakov, M. Burghammer, M. v. Zimmermann, M. Sprung, and A. Ricci, Nature (London) **525**, 359 (2015).
[25] T. Jaouen, B. Hildebrand, M.-L. Mottas, M. Di Giovannantonio, P. Ruffieux, M. Rumo, C. W. Nicholson, E. Razzoli, C. Barreteau, A. Ubaldini, E. Giannini, F. Vanini, H. Beck, C. Monney, and P. Aebi, Phys. Rev. B **100**, 075152 (2019).
[26] A. Kogar, de la Pena, G. A., S. Lee, Y. Fang, S. X.-L. Sun, D. B. Lioi, G. Karapetrov, K. D. Finkelstein, J. P. C. Ruff, P. Abbamonte, and S. Rosenkranz, Phys. Rev. Lett. **118**, 027002 (2017).
[27] Z. Du, H. Li, S. H. Joo, E. P. Donoway, J. Lee, J. C. S. Davis, G. Gu, P. D. Johnson, and K. Fujita, Nature (London) **580**, 65 (2020).
[28] J. V. Badding, J. F. Meng, and D. A. Polvani, Chem. Mater. **10**, 2889 (1998).
[29] E. Gati, L. Xiang, S. L. Bud'ko, and P. C. Canfield, Ann. Phys. (NY) **532**, 2000248 (2020).
[30] A. Saitoh, T. Komatus, T. Kurasawa, H. Ohtake, and T. Suemoto, Phys. Status Solidi **226**, 357 (2001).
[31] A. Lefebvre, Y. Androussi, and G. Vanderschaeve, Phil. Mag. Lett. **56**, 135 (1987).
[32] S. Leoni, R. Ramlau, K. Meier, M. Schmidt, and U. Schwarz, Proc. Natl. Acad. Sci. USA **105**, 19612 (2008).
[33] H. K. Mao, J. Xu, and P. M. Bell, J. Geophys. Res. **91**, 4673 (1986).
[34] K. Syassen, High Pressure Res. **28**, 75 (2008).
[35] M. J. Hytch, Microsc. Microanal. Microstruct. **8**, 41 (1997).
[36] A. K. Gutakovskii, A. L. Chuvilin, and S. A. Song, Bull. Russ. Acad. Sci. Phys. **71**, 1426 (2007).
[37] See Supplemental Material at http://link.aps.org/supplemental/10.1103/PhysRevB.104.125106 for details about sample preparation and experimental details, which includes Ref. [57].
[38] R. Hovden, A. W. Tsen, P. Liu, B. H. Savitzky, I. El Baggari, Y. Liu, W. Lu, Y. Sun, P. Kim, A. N. Pasupathy, and L. F. Kourkoutis, Proc. Natl. Acad. Sci. USA **113**, 11420 (2016).
[39] I. El Baggari, B. H. Savitzky, A. S. Admasu, J. Kim, S.-W. Cheong, R. Hovden, and L. F. Kourkoutis, Proc. Natl. Acad. Sci. USA **115**, 1445 (2018).
[40] D. Walkup, B. A. Assaf, K. L. Scipioni, R. Sankar, F. Chou, G. Chang, H. Lin, I. Zeljkovic, and V. Madhavan, Nat. Commun. **9**, 1550 (2018).
[41] Y. Liu, Y. Y. Li, S. Rajput, D. Gilks, L. Lari, P. L. Galindo, M. Weinert, V. K. Lazarov, and L. Li, Nat. Phys. **10**, 294 (2014).
[42] D. Feinberg and J. Friedel, J. Phys. France **49**, 485 (1988).
[43] J. C. Gill, Phys. Rev. B **53**, 15586 (1996).
[44] R. Brouwer, Incommensurability in crystal structures, Ph.D. thesis, Rijksuniversitiet Groningen, Netherlands, 1978.
[45] A. Spijkerman, J. L. de Boer, A. Meetsma, G. A. Wiegers, and S. van Smaalen, Phys. Rev. B **56**, 13757 (1997).
[46] M. Kuwabara, M. Tomita, H. Hashimoto, and H. Endoh, Phys. Status Solidi A **96**, 39 (1986).
[47] T. Danz, T. Domröse, and C. Ropers, Science **371**, 371 (2021).
[48] G. Storeck, J. G. Horstmann, T. Diekmann, S. Vogelgesang, G. von Witte, S. V. Yalunin, K. Rossnagel, and C. Ropers, Struct. Dyn. **7**, 034304 (2020).
[49] G. C. Trigunayat, Solid State Ionics **48**, 3 (1991).
[50] M. Farkas-Jahnke, Phase Transitions **43**, 81 (1993).
[51] M. Farkas-Jahnke, Bull. Mineral. **109-1-2**, 69 (1986).
[52] M. Farkas-Jahnke and P. Gacs, Krist. Tech. **14**, 1475 (1979).
[53] S. Amelinckx, J. Phys. Colloq. **35**, C7-1 (1974).
[54] E. Bellec, I. Gonzalez-Vallejo, V. L. R. Jacques, A. A. Sinchenko, A. P. Orlov, P. Monceau, S. J. Leake, and D. Le Bolloc'h, Phys. Rev. B **101**, 125122 (2020).
[55] T. L. Adelman, de Lind van Wijngaarden, M. C., S. V. Zaitsev-Zotov, D. DiCarlo, and R. E. Thorne, Phys. Rev. B **53**, 1833 (1996).
[56] W. L. McMillan, Phys. Rev. B **14**, 1496 (1976).
[57] M. J. Hytch, E. Snoeck, and R. Kilaas, Ultramicroscopy **74**, 131 (1998).